

1-2000

# Entrainment response of bed sediment to time-varying flows

David M. Admiraal

*University of Nebraska- Lincoln*, [dadmiraal2@unl.edu](mailto:dadmiraal2@unl.edu)

Marcelo H. Gracia

*University of Illinois at Urbana-Champaign*

Jose F. Rodriguez

*University of Illinois at Urbana-Champaign*

Follow this and additional works at: <https://digitalcommons.unl.edu/civilengfacpub>

---

Admiraal, David M.; Gracia, Marcelo H.; and Rodriguez, Jose F., "Entrainment response of bed sediment to time-varying flows" (2000). *Civil Engineering Faculty Publications*. 133.

<https://digitalcommons.unl.edu/civilengfacpub/133>

This Article is brought to you for free and open access by the Civil Engineering at DigitalCommons@University of Nebraska - Lincoln. It has been accepted for inclusion in Civil Engineering Faculty Publications by an authorized administrator of DigitalCommons@University of Nebraska - Lincoln.

## Entrainment response of bed sediment to time-varying flows

David M. Admiraal,<sup>1</sup> Marcelo H. García, and José F. Rodríguez

Hydrosystems Laboratory, Department of Civil and Environmental Engineering  
University of Illinois at Urbana-Champaign

**Abstract.** Unsteady flows are ubiquitous in nature. In order to understand the behavior of sediment when subjected to unsteady flows, a set of experiments was performed in a rectangular duct with a mobile bed. A computer-operated valve governed the velocity of the water in the duct, and the flow velocity, wall shear stress, and vertical distribution of suspended sediment were simultaneously measured. Beds composed of 120  $\mu\text{m}$  and 580  $\mu\text{m}$  diameter sand were investigated. Both quasi-steady flows and pulse flows were simulated in the duct. For the pulse flows the water was accelerated at a constant rate to a peak velocity and then decelerated at a constant rate to zero velocity. Phase lags were observed between the bed shear stress and the upward flux (entrainment) of sand from the bed. The phase lags were larger for tests with fine sand than for tests with coarse sand. Differences were attributed to differences in bed roughness and flow Reynolds numbers. Relations based on flow acceleration and sediment size were developed for predicting the entrainment phase lag. Large phase lags can have a considerable impact on the amount of sediment transported by boat wakes, waves, and other unsteady flows.

### 1. Introduction

Past sediment transport research has focused primarily on steady flows. However, a number of important sediment transport problems occur in unsteady flows. Examples include sediment transport by boat wakes, waves, and flow surges. For steady flows, entrainment rate relations are available for predicting the upward flux of sediment from a mobile bed, but as flow unsteadiness increases, the reliability of such relations becomes doubtful. Since many natural and man-made flows are unsteady, it is important to determine the applicability of existing relations to unsteady flows and, if necessary, to develop an entrainment relation that can be used in unsteady flows. If a new relation is necessary, it should also be applicable to the more specific case of steady flows.

The main motivation of the research presented herein is to improve estimates of the amount of sediment entrained by barge tows. Bed sediment entrained by tows can be deposited in fragile wetlands or in areas that already require extensive dredging, and in some locations bed sediment contains contaminants, the release of which degrades water quality. Experiments presented herein are meant to simulate wakes and are not periodic, but a review of periodic flow research suggests that the two types of flows have similar characteristics. Results of the experiments relate sediment entrainment to unsteady bed shear stresses and provide insight into the behavior of sediment in a variety of periodic and nonperiodic unsteady flows.

### 2. Background

For calculating suspended sediment concentration profiles, a near-bed boundary condition is required. In steady, uniform

flows either sediment flux or concentration may be specified near the bed. A number of researchers, including *Parker* [1978], *Nielsen* [1988], and *Davies* [1995], maintain that for nonequilibrium and unsteady flows the sediment flux is the most appropriate boundary condition since sediment in suspension cannot instantaneously respond to changes in flow conditions or bed attributes. For example, if bed shear stress goes to zero, a concentration boundary condition immediately requires the near-bed concentration to be zero, and a flux boundary condition requires the upward flux of sediment from the bed to be zero. Only the second boundary condition is possible since the near-bed concentration cannot be zero until all of the sediment in suspension falls to the bed. The downward component of the sediment flux at the bed is generally taken to be the product of the near-bed concentration and the sediment fall velocity. The upward component of the flux is dependent on flow conditions and sediment properties and is called the entrainment rate or pick-up function. The dimensionless entrainment rate is obtained by dividing the entrainment rate by the sediment fall velocity.

For steady flows, *García and Parker* [1991] have shown that the dimensionless entrainment rate ( $E_s$ ) can be represented as

$$E_s = f_1 \left( \frac{u_*}{\sqrt{gRD_s}}, \frac{H}{D_s}, R_{ep}, R \right), \quad (1)$$

where  $u_*$  is the shear velocity due to skin friction,  $g$  is the gravitational acceleration,  $R$  is the submerged specific gravity of the sediment (the specific gravity of the sediment minus the specific gravity of water),  $D_s$  is the mean sediment diameter, and  $H$  is the flow depth.  $R_{ep}$  is the particle Reynolds number and is given as

$$R_{ep} = D_s \sqrt{gRD_s} / \nu, \quad (2)$$

where  $\nu$  is the kinematic viscosity of the water. For most cases of interest,  $R$  is constant (1.65 for quartz). In addition, *García and Parker* found that the relative roughness ( $D_s/H$ ) does not significantly affect entrainment. Thus (1) can be rewritten

<sup>1</sup>Now at Department of Civil Engineering, University of Nebraska at Lincoln.

$$E_s = f_2 \left( \frac{u_*}{\sqrt{gRD_s}}, R_{ep} \right). \quad (3)$$

Most empirical relations that predict the near-bed concentration or entrainment rate are given as a function of the two parameters in (3). Examples include the formulas of *Einstein* [1950], *Engelund and Fredsøe* [1976, 1982], *Smith and McLean* [1977], *Itakura and Kishi* [1980], *van Rijn* [1984], *Celik and Rodi* [1984], *Akiyama and Fukushima* [1986], *García and Parker* [1991], and *Zyserman and Fredsøe* [1994]. *García and Parker* [1991] provided a detailed analysis of most of these relations using an extensive set of laboratory and field measurements; they determined that of all the relations those of *Smith and McLean* [1977], *van Rijn* [1984], and *García and Parker* [1991] performed the best.

An added advantage of the *García-Parker* relation is that it is easily applied to unsteady flows [*Admiraal*, 1999]; therefore the relation is used to calculate the sediment entrainment rates reported in this paper. The relation estimates the entrainment rate of uniformly sized sand at a reference elevation of 1/20 of the flow depth and is given as

$$E_s = AZ_u^5 / \left( 1 + \frac{A}{0.3} Z_u^5 \right), \quad (4)$$

where  $A$  is equal to  $1.3 \times 10^{-7}$  and the entrainment parameter ( $Z_u$ ) is

$$Z_u = \frac{u_*}{v_s} R_{ep}^{0.6}, \quad (5)$$

where  $v_s$  is the fall velocity of the sediment particles.

Entrainment of sediment into suspension is caused by turbulence. Using flow visualization techniques, *Sutherland* [1967] and *Niño and García* [1996] demonstrated the entrainment of sediment by turbulent ejections of near-wall fluid. Other researchers, including *Soulsby et al.* [1987] and *Lapointe* [1992], have shown strong correlation between turbulent events and the entrainment of sediment. Equation (3) is valid in steady flows because turbulence parameters are in equilibrium and the intensity of the turbulence is related to the shear velocity. In unsteady flows the turbulence is not in equilibrium, and the validity of (3) depends on whether or not the shear velocity and the turbulent processes responsible for entraining the sediment are related.

For oscillatory pipe flows, *Mizushima et al.* [1975] and *Ramaprian and Tu* [1982] describe a phase lag between the wall shear stress and turbulence properties (i.e., Reynolds stress and turbulence intensity). The phase lag of the turbulence properties increases with distance from the wall. In unsteady flows a phase lag between the wall shear stress and entrainment can also be expected since turbulent events are responsible for entrainment. Existing entrainment relations may need to be modified to account for the lag. Most sediment can react to relatively rapid turbulent bursts, and the response time of sediment does not appear to be responsible for phase lags between the wall shear stress and entrainment. It is more likely that delays in the production and propagation of turbulence cause delays in the entrainment and vertical transport of the sediment. There is also a phase lag between the wall shear stress and cross-sectional average velocity, but for turbulent flows it is often much smaller than the phase lag between the wall shear stress and turbulence properties.

A number of researchers, including *Davies* [1995], *Nielsen*

[1988, 1992], and *Horikawa et al.* [1982], have explored wave-related sediment entrainment. Oscillatory flows with suspended sediment investigated by *Nielsen* [1992] and *Horikawa et al.* [1982] show a phase difference between the peak velocity and the peak sediment concentration at various heights above the bed. Like the phase lag of turbulence parameters, the phase lag of peak concentration increases with distance from the bed. The phase difference between peak concentration and peak velocity is important for the computation of suspended load. The streamwise flux of suspended sediment is equal to the product of velocity and concentration. Clearly, suspended sediment transport will be greatest if the peak sediment concentration coincides with the peak velocity. In some combined wave-current flows, phase differences between sediment concentrations and flow velocities are so large that sediment is transported in the opposite direction as the average flow velocity [*Nielsen*, 1988; *Inman and Bowen*, 1962].

### 3. Sediment Mass Balance Equations

The species conservation equation governs the entrainment of sediment from a moveable bed. For steady flows, instantaneous parameters are usually separated into mean and random fluctuating quantities, and conservation equations are time averaged in order to separate turbulence properties from mean flow characteristics. For time-varying flows, time averaging is replaced by ensemble averaging, and instantaneous velocities ( $u_i$ ) and concentration ( $c$ ) are separated into ensemble-averaged and random fluctuating quantities:

$$u_i = \bar{u}_i + u'_i \quad (6)$$

$$c = \bar{c} + c', \quad (7)$$

where  $\bar{u}_i$  and  $\bar{c}$  are ensemble-averaged velocities and concentration, respectively, and  $u'_i$  and  $c'$  are random (or turbulent) components of velocities and concentration, respectively. For the data presented in this paper, turbulence timescales are much shorter than the timescales of ensemble-averaged quantities.

If molecular diffusion is neglected and suspended sediment is assumed to follow the flow velocity except for a constant fall velocity in the downward direction, the ensemble-averaged species conservation equation is

$$\frac{\partial \bar{c}}{\partial t} + \frac{\partial F_i}{\partial x_i} = 0, \quad (8a)$$

where  $F_i$  represents sediment fluxes in the three principle directions:

$$F_1 = \bar{u}_1 \bar{c} + \langle u'_1 c' \rangle \quad (8b)$$

$$F_2 = \bar{u}_2 \bar{c} + \langle u'_2 c' \rangle \quad (8c)$$

$$F_3 = (\bar{u}_3 - v_s) \bar{c} + \langle u'_3 c' \rangle, \quad (8d)$$

$x$  and  $t$  indicate direction and time, respectively, and the indices one, two, and three represent the streamwise, spanwise, and vertical directions, respectively. The flows presented herein are two-dimensional, so that the spanwise component of the sediment flux ( $F_2$ ) is zero, and the control volume shown in Figure 1 applies. The spatial extents of the control volume are  $a_0$ ,  $a_1$ ,  $b_0$ , and  $b_1$ . A dashed line just above the sand bed indicates the height at which entrainment rate is predicted.

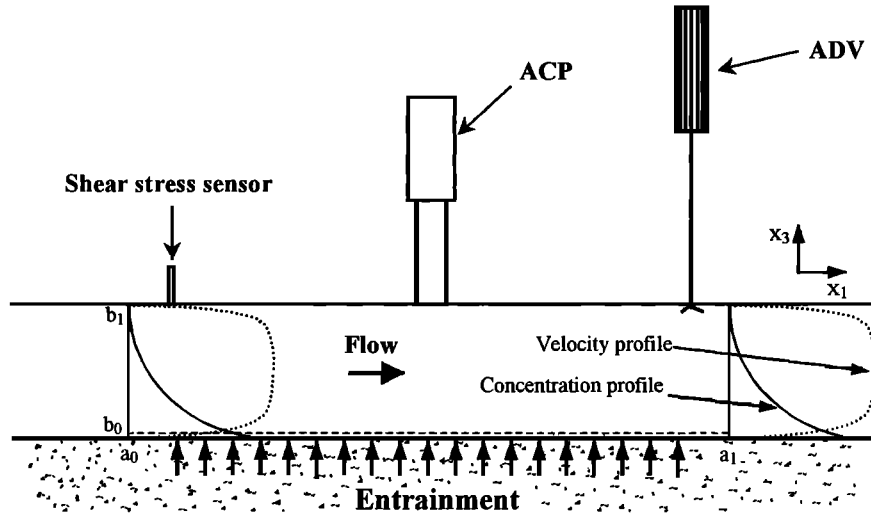


**Figure 1.** Control volume of two-dimensional entrainment. Location of reference level  $b_0$  is shown by the dashed line. Locations of measuring devices are also shown. ACP is Mesotech acoustic concentration profiler.

Figure 1 also shows the locations of sensors used in the experiments. These sensors are discussed in more detail in section 4.

The two-dimensional form of (8a) is integrated over the control volume in time and space and is simplified to form

$$\int_{b_0}^{b_1} \int_{a_0}^{a_1} \bar{c} \Big|_{t_0}^{t_1} dx_1 dx_3 + \int_{t_0}^{t_1} \int_{b_0}^{b_1} F_{1|a_0}^{a_1} dx_3 dt + \int_{t_0}^{t_1} \int_{a_0}^{a_1} F_{3|b_0}^{b_1} dx_1 dt = 0, \quad (9)$$

where  $t_0$  and  $t_1$  represent the initial and final time of integration. According to (9) the amount of sediment within the control volume depends on the flux of sediment across the control surface. In the present case the flux across the upper surface of the control volume is zero since the upper surface is impervious. The average vertical velocity is zero near the bed, and the vertical flux of sediment at the height  $b_0$  can be simplified to get

$$F_{3|b_0} = (-v_s \bar{c} + \langle u'_3 c' \rangle) \Big|_{b_0} = v_s (-\bar{c} + E_n) \Big|_{b_0}. \quad (10)$$

Here the dimensionless entrainment rate ( $E_n$ ) replaces the ensemble-averaged Reynolds concentration flux. Equations (9) and (10) are combined, and  $E_n$  is solved for to obtain

$$\int_{t_0}^{t_1} \int_{a_0}^{a_1} E_n \Big|_{b_0} dx_1 dt = \left( \frac{1}{v_s} \int_{b_0}^{b_1} \int_{a_0}^{a_1} \bar{c} \Big|_{t_0}^{t_1} dx_1 dx_3 + \frac{1}{v_s} \int_{t_0}^{t_1} \int_{b_0}^{b_1} F_{1|a_0}^{a_1} dx_3 dt + \int_{t_0}^{t_1} \int_{a_0}^{a_1} \bar{c} \Big|_{b_0} dx_1 dt \right). \quad (11)$$

In the present set of experiments the location of the control volume is well downstream of the duct entrance (50 duct heights). In most cases, unsteady flow tests are so short that entrance effects are not felt at the control volume, and steady flow measurements indicate that velocity profiles at the inlet and outlet of the control volume are the same. Suspended sediment profiles also appear to be established at the control

volume, and no bed forms were observed in any of the tests. Since velocity and concentration profiles in the control volume do not vary in the streamwise direction, the flow can be considered uniform, and the streamwise fluxes of sediment into and out of the control volume are the same. Consequently, the second integral on the right-hand side of (11) is zero, yielding

$$\int_{t_0}^{t_1} E_n \Big|_{b_0} dt = \left( \frac{1}{v_s} \int_{b_0}^{b_1} \bar{c} \Big|_{t_0}^{t_1} dx_3 + \int_{t_0}^{t_1} \bar{c} \Big|_{b_0} dt \right). \quad (12)$$

In order to compute entrainment for unsteady, uniform flows, it is necessary to measure both the amount of suspended sediment in the water column and the near-bed concentration as a function of time. For steady, uniform flows the amount of suspended sediment in the control volume is constant, and (12) can be further simplified to get

$$E_n \Big|_{b_0} = \bar{c} \Big|_{b_0}. \quad (13)$$

Equation (13) has been used in the development of most existing entrainment relations. As long as the assumptions used to derive (13) are correct,  $E_s$ ,  $\bar{c} \Big|_{b_0}$ , and  $E_n \Big|_{b_0}$  are the same.

#### 4. Experimental Apparatus

Experiments were performed in the flume shown in Figure 2. The approximate location of the test section (control volume) and pressure taps are indicated in the diagram. The flume consists of a 6 m long rectangular duct made of Plexiglas, a 2 m high head tank, and a large tail box. The duct has a false floor that can be removed and replaced with a sand bed. The sand bed is about 12.5 cm thick, and the flow area above the sand bed is 30 cm wide and 10 cm high. Sand is not recirculated within the duct, and a scour hole develops at the entrance of the duct. The scour hole is far enough upstream of the test section so that test results are not affected, and the scour hole is regularly filled in so that the bed elevation in the duct remains constant.

Water is supplied to the head tank by the laboratory pumps, and an overflow weir holds the inlet head nearly constant at

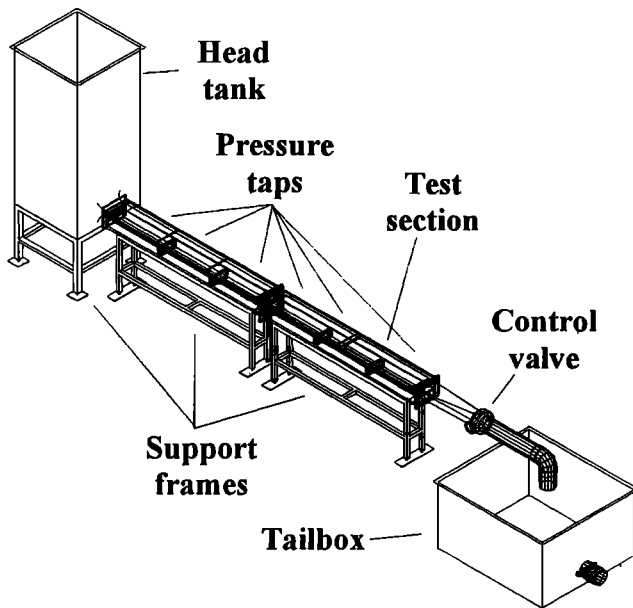


Figure 2. Isometric view of the experimental entrainment flume.

2 m above the duct centerline. At the downstream end of the channel the outlet head is controlled with a computer-operated valve. The computer used to open and close the valve also provides synchronization for the measuring devices so that multiple realizations can be ensemble averaged.

The duct has 12 pressure taps spaced at 0.5 m intervals for measuring the pressure drop in steady flow conditions. Three sensors are used in the experiments: a TSI 1237W hot film shear stress sensor, a Mesotech acoustic concentration profiler (ACP), and a Sontek acoustic doppler velocimeter (ADV). As depicted in Figure 1, the sensors are spaced 0.5 m apart within the control volume. Physical constraints prevented the sensors from being mounted at the same streamwise location, but as long as the flow within the control volume is uniform, ensemble-averaged flow measurements do not vary in the streamwise direction.

The shear stress sensor measures shear stress on the ceiling (or upper surface) of the duct and has been calibrated in situ over a wide range of steady flow conditions. These sensors have been successfully used to measure shear stresses in both steady [e.g., García *et al.*, 1995; Admiraal, 1997] and unsteady [e.g., Menendez and Ramaprian, 1985; Rodríguez, 1997] flows. The ACP measures entire vertical profiles of sediment concentration, but its output is a function of sediment size, and it must be calibrated for each size investigated [Hay, 1991]. The ACP was calibrated in a specially designed facility in which ACP measurements were compared with isokinetic suction samples. During steady flow tests, samples were also gathered in the experimental duct at heights of 1.1, 2.1, and 3.1 cm above the bed. For steady flow tests with 120  $\mu\text{m}$  diameter sand, agreement between samples and ACP measurements was good, with maximum differences of about 15%. Agreement between samples and measurements was not as good for tests with 580  $\mu\text{m}$  diameter sand. Except near the bed, concentrations of the 580  $\mu\text{m}$  sand are quite low, and the ACP is not as accurate for low concentrations. Measurement uncertainties associated with the ACP were about 10% and 15% for 120  $\mu\text{m}$  and 580  $\mu\text{m}$

diameter sands, respectively. The ADV measures velocity at the centerline of the duct and does not require calibration. More details about calibration of the shear stress sensor and the ACP are given by Admiraal [1999] and Admiraal and García [1999].

## 5. Measurement of Bed Shear Stress

For the unsteady flows presented herein, bed shear stress cannot be directly measured. Since high sediment concentrations obstruct near-bed velocity measurements, the bed shear stress cannot be computed from velocity profiles. An alternative method of determining bed shear stress uses pressure drop and shear stress sensor measurements on the ceiling of the duct. According to Rouse [1961], pressure drop measurements in a wide, horizontal, rectangular duct with a smooth upper surface can be used to compute the shear stress on a bottom surface of unknown roughness [see also Schlichting, 1936].

The combined shear stress imparted on the flow by the duct walls is calculated from pressure drop measurements. A force balance is applied to an isolated section of the rectangular duct (where the flow is fully developed) to obtain

$$\tau_{0,s} + \tau_{0,r} = -h \frac{\partial P}{\partial x}, \quad (14)$$

where  $\tau_{0,s}$  is the shear stress on the smooth surface,  $\tau_{0,r}$  is the shear stress on the rough wall,  $h$  is the height of the duct,  $P$  is the pressure head, and  $x$  is the streamwise coordinate. Since the aspect ratio of the experimental duct is only 3:1, (14) was modified to include shear stress on the side walls; the result is

$$\left(\frac{2h+b}{b}\right)\tau_{0,s} + \tau_{0,r} = -h \frac{\partial P}{\partial x}, \quad (15)$$

where  $b$  is the width of the duct.

Equation (15) has been used to calculate the bed shear stress for a range of steady flow tests. In Figure 3 the bed shear stress is plotted against the shear stress measured on the ceiling of the duct for 120  $\mu\text{m}$  and 580  $\mu\text{m}$  diameter sediment beds. There appears to be a linear relationship between the two shear stresses. When the bed is 120  $\mu\text{m}$  sand, the ratio of the bed shear stress to the wall shear stress is 1; when the bed is 580  $\mu\text{m}$  sand, the ratio is 1.5. Curves representing these two ratios are shown in Figure 3.

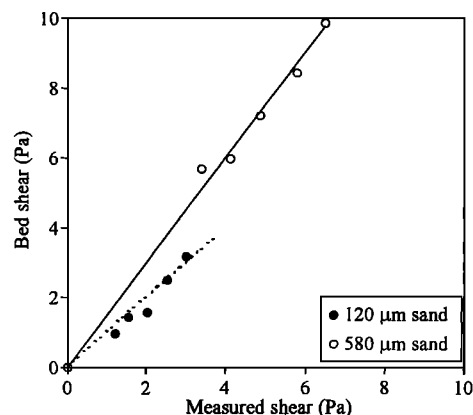


Figure 3. Comparison of bed shear stress and measured shear stress.

According to *Nezu and Nakagawa* [1993] a surface is hydraulically smooth as long as the dimensionless roughness ( $k_s^+$ ) is less than 5. Here  $k_s^+$  is given by

$$k_s^+ = \frac{k_s}{\nu/u_*}, \quad (16)$$

where  $k_s$  is the bed roughness (set equal to the sand grain diameter). For the tests with 120  $\mu\text{m}$  sand the maximum shear velocity is approximately 0.05 m/s, and the maximum value of  $k_s^+$  is about 5. Thus the 120  $\mu\text{m}$  sand bed is hydraulically smooth, and it is not surprising that bed shear stress is the same as the shear stress measured on the smooth duct ceiling. During tests with the 580  $\mu\text{m}$  sand, peak shear velocities are as high as 0.07 m/s, and the peak value of  $k_s^+$  is about 40, corresponding to a transitionally rough bed (for a completely rough bed  $k_s^+ > 70$ ).

The pressure drop could not be measured during unsteady flow tests because the time response of the pressure transducer was limited and the transducer was susceptible to water hammer damage. Instead, it was assumed that the ratio of bed shear stress to measured shear stress is the same for unsteady flows and steady flows. Measured shear stresses could then be multiplied by the ratio to get the shear stress on the bed. The bed is hydraulically smooth for all of the unsteady flow tests with 120  $\mu\text{m}$  sand, and it is reasonable to assume that the measured shear stress and the bed shear stress are the same. In unsteady flow tests with 580  $\mu\text{m}$  sand, it is less likely that the ratio between measured shear stress and bed shear stress is fixed since the bed is transitionally rough. However, no other method is available for measuring time-varying shear stress on the 580  $\mu\text{m}$  sand bed.

## 6. Experiments

Two sets of experimental data are presented in this paper, both consisting of flows above a plane bed composed of loose sand. For tests in the first data set the velocity in the duct is increased from zero to a plateau velocity and is then held steady. Only measurements taken after the velocity reaches its plateau are used in the analysis. Table 1 gives details of the tests in the first data set including sand diameter, centerline velocity,  $Re_h$  (flow Reynolds number based on centerline velocity and duct height), shear velocity, and dimensionless entrainment rate.

In Figure 4, measured entrainment rates are plotted as a function of the entrainment parameter  $Z_u$ . The measured data appear to be in agreement with the Garcia-Parker relation.

**Table 1.** Quasi-Steady Test Conditions

Test	Sand Diameter, $\mu\text{m}$	Centerline Velocity, cm/s	$Re_h$	Shear Velocity, m/s	Entrainment Rate
1a	120	69.0	$6.27 \times 10^4$	0.031	0.0085
1b	120	78.7	$7.15 \times 10^4$	0.038	0.0132
1c	120	90.4	$8.22 \times 10^4$	0.040	0.0223
1d	120	101.8	$9.25 \times 10^4$	0.050	0.0368
1e	120	112.7	$1.02 \times 10^5$	0.056	0.0530
2a	580	120.3	$1.09 \times 10^5$	0.075	0.0049
2b	580	134.4	$1.22 \times 10^5$	0.077	0.0093
2c	580	147.2	$1.34 \times 10^5$	0.085	0.0157
2d	580	161.9	$1.47 \times 10^5$	0.092	0.0194
2e	580	173.3	$1.58 \times 10^5$	0.099	0.0274

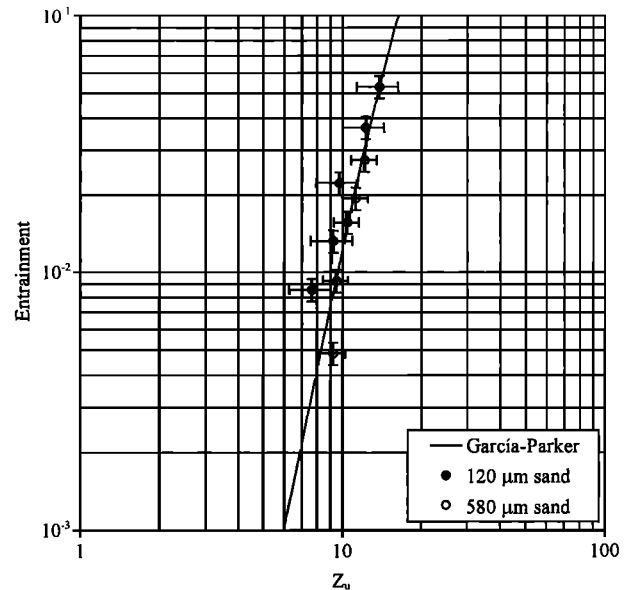


**Figure 4.** Entrainment results of steady flow tests plotted against Garcia-Parker relation.

Measurement uncertainties associated with  $Z_u$  and  $E_s$  are also shown in Figure 4. The uncertainties were calculated using the standard error method [Admiraal, 1999] and are typical of those observed in all of the steady and unsteady flow experiments.

The second data set was collected to investigate the behavior of suspended sediment in unsteady flows. The data set consists of flows in which the velocity in the duct was accelerated from zero to a peak velocity and was then decelerated back to zero. Since acceleration and deceleration rates are approximately constant, the velocity pulses in the second data set have a triangular shape. Information about the second data set is given in Table 2. Note that in Table 2, the magnitude of  $Re_w$  varies because of differences in both water temperature and sediment size.  $Re_w$  (the wave Reynolds number) and  $A_w$  (a dimensionless acceleration that indicates how rapidly the shear velocity changes with time) are also given in Table 2. The wave Reynolds number has been given by *Fredsøe and Deigaard* [1992] as

$$Re_w = \frac{U_m^2 T}{2\pi\nu}. \quad (17)$$

For periodic waves,  $U_m$  is the amplitude of the oscillatory velocity, and  $T$  is the period of the velocity wave. The velocity pulses described herein are not periodic; therefore  $T$  represents the pulse duration, and  $U_m$  represents half of the peak velocity (as though the pulse was one cycle of a periodic wave). The dimensionless acceleration  $A_w$  is

$$A_w = \frac{\nu}{(gRD_s)^{3/2}} \frac{4\bar{u}_*}{T}, \quad (18)$$

where  $\bar{u}_*$  is the shear velocity time averaged over the pulse duration.

For unsteady pulse flows the phase lag of the entrainment is dependent on variables similar to those given by (3). However, for pulse flows,  $u_*$  varies with time, and phase lag is a function of the distribution of shear velocity over the entire pulse (not

**Table 2.** Pulse Flow Test Conditions

Test	Sand Diameter, $\mu\text{m}$	$R_{ep}$	Number of Realizations	Peak Velocity, cm/s	Velocity Pulse Duration, s	$A_w$	$Re_w$	$\Delta t_p$ , s	$\Delta t_c$ , s
3a	120	4.85	60	101	7.5	$1.3 \times 10^{-4}$	$2.79 \times 10^5$	0.7	0.94
3b	120	4.85	60	104	15.0	$7.4 \times 10^{-5}$	$5.92 \times 10^5$	0.6	1.24
3c	120	6.11	100	96	3.45	$2.5 \times 10^{-4}$	$1.46 \times 10^5$	0.6	0.55
3d	120	6.05	100	142	4.6	$2.3 \times 10^{-4}$	$4.22 \times 10^5$	0.5	0.64
3e	120	6.09	100	139	2.72	$3.9 \times 10^{-4}$	$2.41 \times 10^5$	0.5	0.70
4a	580	52.5	60	186	4.39	$4.6 \times 10^{-5}$	$5.65 \times 10^5$	0.3	0.10
4b	580	54.0	80	141	7.9	$1.8 \times 10^{-5}$	$6.01 \times 10^5$	0.4	0.15
4c	580	52.5	60	153	15.7	$9.9 \times 10^{-6}$	$1.37 \times 10^6$	0.4	0.34

just the ensemble-averaged shear velocity). For instance, *Ramaprian and Tu* [1982] showed that the propagation time of turbulence in an oscillatory flow is correlated to the time-averaged shear velocity. Consequently,  $\bar{u}_*$  is used instead of  $u_*$  for characterizing phase lag. Furthermore, the pulse duration ( $T$ ) is introduced to represent the unsteadiness of the pulse flow. One possible combination of dimensionless numbers is

$$\phi_E = f_3 \left( \frac{\bar{u}_*}{\sqrt{gRD_s}}, R_{ep}, \frac{TgRD_s}{\nu} \right), \quad (19)$$

where  $\phi_E$  represents the phase lag of the entrainment. Taking the ratio of the first and third terms given on the right-hand side of (19) yields

$$\frac{\nu}{(gRD_s)^{3/2}} \frac{\bar{u}_*}{T} = \frac{1}{4} A_w. \quad (20)$$

Then (19) can be rewritten as

$$\phi_E = f_4(A_w, R_{ep}), \quad (21)$$

which gives the phase lag as a function of shear velocity acceleration and particle size.

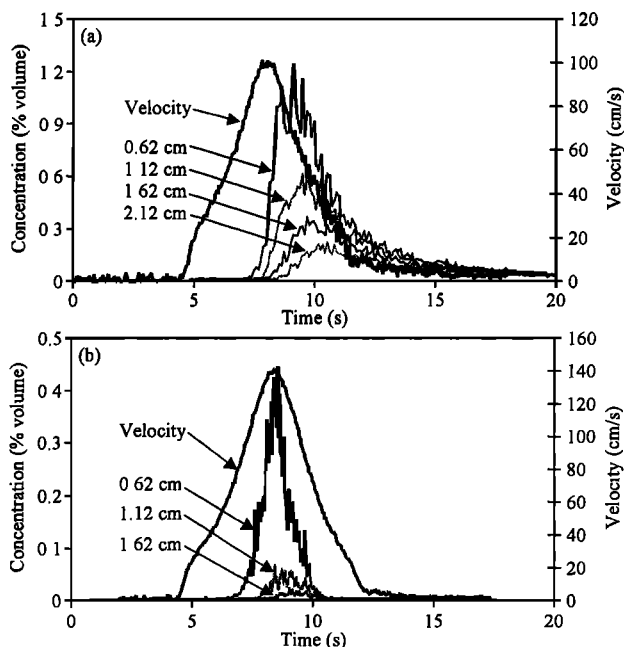


**Figure 5.** Time series of centerline velocity and concentration at various elevations for (a) test 3a and (b) test 4b. Elevations of concentration measurements are given.

Centerline velocity, wall shear stress, and sediment concentration profiles were measured as a function of time for all of the tests shown in Table 2. Time series of the centerline velocity and the sediment concentration at several heights above the bed are given in Figure 5 for tests 3a and 4b. There is an obvious time lag between peak centerline velocity and peak concentration for the test shown in Figure 5a, and time lags are greater for concentrations farther from the bed. The phase difference between centerline velocity and bed shear stress is small for all of the tests, and peak concentrations of suspended sediment also lag behind the peak bed shear stress. Figure 5a also shows that the 120  $\mu\text{m}$  sand does not immediately fall out of suspension after the velocity pulse passes. The sand takes significantly longer to settle than predicted using its terminal fall velocity. The turbulence in the duct does not dissipate immediately and keeps the sediment suspended long after the average bed shear stress drops to zero.

Figure 5b shows that there is also a time lag between peak centerline velocity and peak concentrations of 580  $\mu\text{m}$  sand. However, the time lags observed for the 580  $\mu\text{m}$  sand are not nearly as large as they are for the 120  $\mu\text{m}$  sand. In addition, the 580  $\mu\text{m}$  sand falls out of suspension almost immediately after the flow decelerates, suggesting that the high turbulence levels necessary to keep the 580  $\mu\text{m}$  sand suspended dissipate rapidly.

In unsteady flows the entrainment rate and the near-bed concentration are related but not equal; both the near-bed concentration and the rate of change of the amount of sediment in suspension must be measured to determine the entrainment rate. In Figure 6 the near-bed concentration and the rate of change of sediment in suspension (volumetric flux) are given as a function of time for test 3a. The entrainment rate,

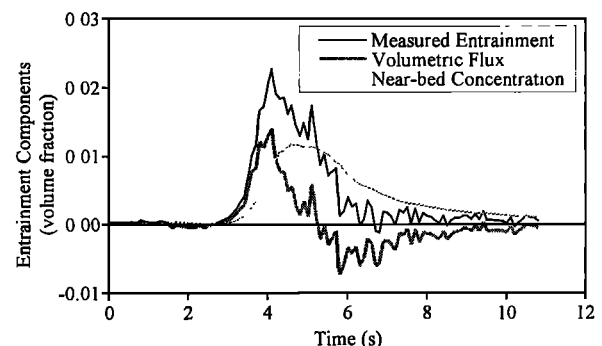


**Figure 6.** Entrainment and components of entrainment resulting from the velocity pulse of test 3a.

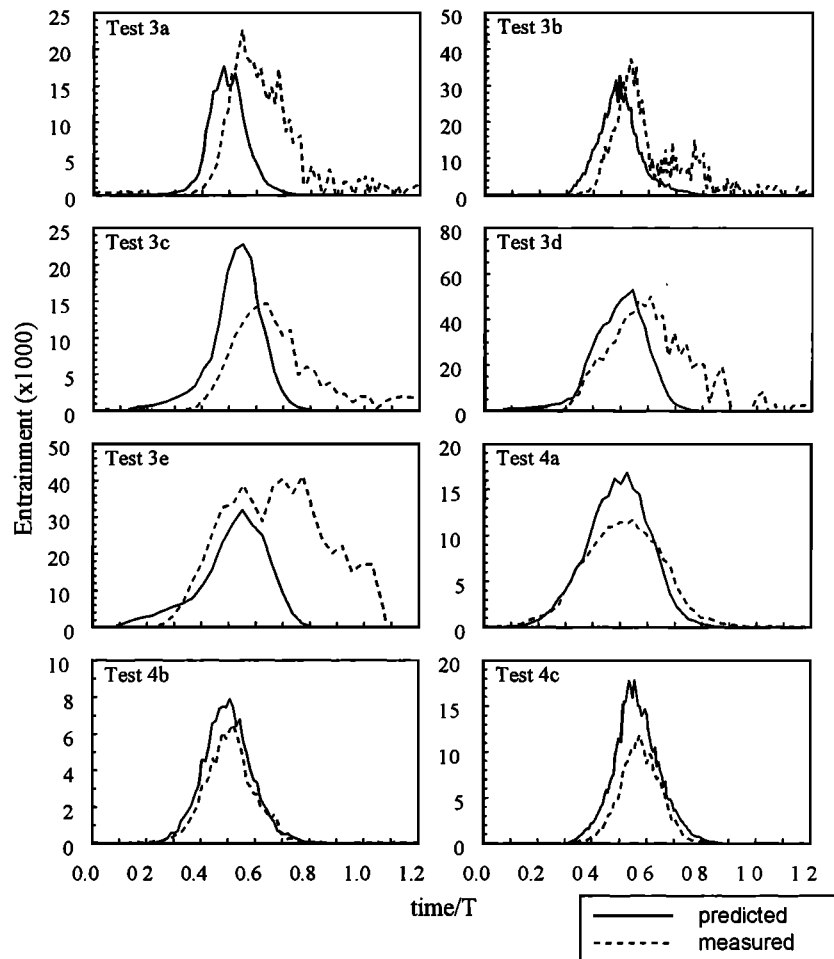


Figure 7. Comparison of predicted and measured entrainment time series for unsteady pulse tests.

which is given by (12) as the sum of the near-bed concentration and the volumetric flux, is also shown in Figure 6.

If the rate of change of the amount of suspended sediment has a different time lag than the near-bed concentration, the time lags of the entrainment rate and the near-bed concentration are also different. Vertical concentration profiles are much steeper for coarse sand than for fine sand, and a much higher percentage of the coarse sand that is suspended travels near the bed. Consequently, the time lag of entrainment resembles the time lag of near-bed concentration more closely for coarse sediment than for fine sediment.

Figure 7 shows the predicted and measured entrainment rate time series of each of the tests in Table 2. Equations (4) and (5) and shear stress measurements corresponding to each test are used to predict the entrainment rate. The measured entrainment rate is computed using (12) and the sediment concentration measurements. The measured and predicted entrainment rates shown in Figure 7 are generally in agreement except for a time lag between them. The time lag is a result of the time lag between bed shear stress and concentration measurements.

The total volume of sediment per unit area of bed that is entrained by a velocity pulse is calculated by integrating the entrainment rate over the pulse duration. Total entrainment amounts (per unit area of bed) have been calculated for each test using both predicted and measured entrainment rates;

these amounts are given in Table 3 for each of the pulse tests. Considering the steep slope of the García-Parker relation (shown in Figure 4), the limited accuracy of the results given in Table 3 is not unexpected, and as suspended sediment transport relations go, (4) and (5) perform quite well.

Measured entrainment rates are higher than expected during flow deceleration, and in some tests  $120\ \mu\text{m}$  sand remains suspended well after the average bed shear stress drops to zero. Consequently, the total predicted entrainment is less than the total measured entrainment in all of the  $120\ \mu\text{m}$  tests. There are two possible explanations for the high values of measured entrainment. The first explanation is that the terminal fall velocity of the sand is reduced by residual turbulence. When the fall velocity used in (12) is incorrect, entrainment rate calculations are erroneous. If fall velocity is reduced, the actual entrainment is less than the entrainment that was measured. The second explanation is that residual turbulence continues to entrain sediment even after the average bed shear stress drops to zero (experiments performed by Rouse [1939], in which sediment was entrained by an oscillating grid, are a good example of entrainment that occurs with an average bed shear stress of zero); in this case, (4) and (5) do not adequately predict the total entrainment.

There is disagreement about the effect that turbulence has on fall velocity. Experiments by Boillat and Graf [1982] and computer simulations by Wang and Maxey [1993] demonstrate

**Table 3.** Comparison of Measured and Predicted Total Entrainment and Sediment Load

Test	Total Volume of Sediment Entrained per Unit Area of Bed			$Q_s$ Computed for Various Boundary Conditions			$Q_s$ Measured, kg/m
	Measured, $m^3/m^2$	Predicted, $m^3/m^2$	Difference, %	Near-Bed Concentration, kg/m	Entrainment, kg/m	Time-Delayed Entrainment, kg/m	
3a	$4.5 \times 10^{-4}$	$2.2 \times 10^{-4}$	51	0.64	0.52	0.44	0.62
3b	$1.0 \times 10^{-3}$	$7.9 \times 10^{-4}$	24	2.56	2.25	2.03	2.20
3c	$1.9 \times 10^{-4}$	$1.7 \times 10^{-4}$	11	0.42	0.30	0.23	0.16
3d	$8.1 \times 10^{-4}$	$5.8 \times 10^{-4}$	28	2.53	1.75	1.49	1.52
3e	$5.3 \times 10^{-4}$	$2.4 \times 10^{-4}$	54	0.86	0.57	0.52	0.73
4a	$1.6 \times 10^{-3}$	$1.8 \times 10^{-3}$	9	...	...	...	...
4b	$9.1 \times 10^{-4}$	$1.1 \times 10^{-3}$	23	...	...	...	...
4c	$2.8 \times 10^{-3}$	$4.4 \times 10^{-3}$	58	...	...	...	...

Ellipsis indicates total loads were not computed for coarse sediment since the numerical model is only accurate for fine sediment calculations.

that the fall velocity of a sphere increases in homogeneous, isotropic turbulence. Wang and Maxey predicted increases in fall velocity as high as 50%. However, Murray [1970] found that fall velocities of 2 mm spheres were reduced when subjected to grid generated turbulence and conjectured that the fall velocity of 350  $\mu\text{m}$  particles could be reduced by as much as 30% in large rivers. Data collected by Ludwick and Domurat [1982] indicated that the fall velocity of 100 and 200  $\mu\text{m}$  particles was not strongly influenced by turbulence. In the present case it is not clear how turbulence affects the fall velocity of the sand, but even a reduction in fall velocity of 30% cannot account for differences between measured and predicted entrainment rates [Admiraal, 1999]. Thus, during deceleration, entrainment rates predicted using (4) and (5) are low, and it is likely that residual turbulence augments entrainment rates.

## 7. Prediction of Time Lags

### 7.1. Phase Lags of Peak Concentration Measurements

The time lags of peak concentration after peak shear stress have been determined for all of the tests in Table 2. Time lags were converted to phase lags (in degrees) by dividing the time lag by the pulse duration and multiplying by 360°. The phase lag of peak concentration ( $\phi_c$ ) is plotted as a function of the dimensionless elevation ( $\eta$ ) in Figure 8. Value  $\eta$  equals  $2y/h$ , and  $y$  is the elevation above the bed ( $h/2$  is the characteristic length of the duct since the boundary layer thickness is half of the duct height).

In Figure 8, phase lags of the near-bed concentration vary between 10° and 90°. Davies [1995] suggests that for oscillatory flow over a plane bed, the phase lag of the near-bed concentration is roughly 40°. Most of the tests with the fine sand support this estimate. However, test 3e (which has the highest acceleration) has a phase lag of 90°, and the coarse sand tests have phase lags of about 10°. The phase lags of near-bed concentration and entrainment rate are affected by the same dimensionless parameters. In Figure 9a, phase lag of the peak near-bed concentration ( $\phi_{nb}$ ) is plotted against  $A_w$ . Value  $\phi_{nb}$  increases with increasing acceleration for the 120  $\mu\text{m}$  sand but is relatively constant for the 580  $\mu\text{m}$  sand. Phase lags (and time lags) of the near-bed concentrations of 120  $\mu\text{m}$  sand are significantly higher than those of the 580  $\mu\text{m}$  sand even though the inertia of the 120  $\mu\text{m}$  sand is much less. However, particle inertia is not the only difference between the 120  $\mu\text{m}$  tests and the 580  $\mu\text{m}$  tests.

Smaller particles may be immersed in the viscous sublayer

where they can only be dislodged by larger turbulent fluctuations. If development of the viscous sublayer can be treated as quasi-steady, the thickness of the viscous sublayer ( $\delta$ ) can be defined as

$$\delta = 11.6\nu/u_* \quad (22)$$

If the sand diameter is larger than the sublayer thickness, the sand protrudes out of the sublayer. Consequently, the sand will protrude out of the viscous sublayer if

$$D_s > 11.6\nu/u_*; \quad (23)$$

(23) can be modified to show that sand grains protrude if

$$u_*^2/gRD_s > (11.6/R_{ep})^2. \quad (24)$$

The quantity on the left-hand side of (24) is the dimensionless Shields stress. Implications of (24) are demonstrated in Figures 10a and 10b. In Figure 10, 120  $\mu\text{m}$  and 580  $\mu\text{m}$  sand beds are subjected to the same shear stress pulse (shown in Figure 10a). In Figure 10b, Shields stress is given as a function of time for both sand sizes, and the protrusion-immersion boundaries defined by (24) are also shown for both sizes. Though the 580  $\mu\text{m}$  sand protrudes through the viscous sublayer for a majority of

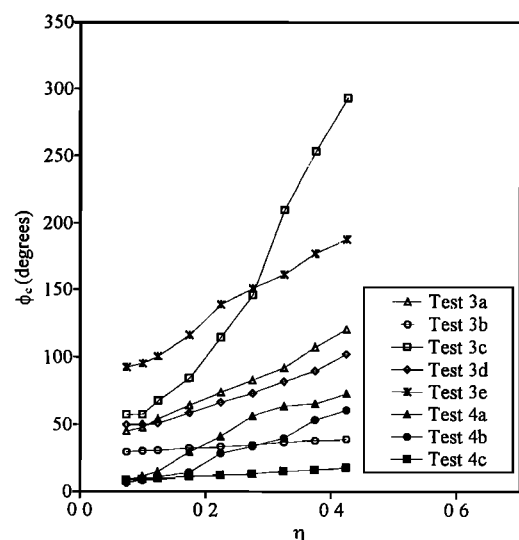


**Figure 8.** Phase lag of peak concentration after peak shear stress for pulse flow tests.

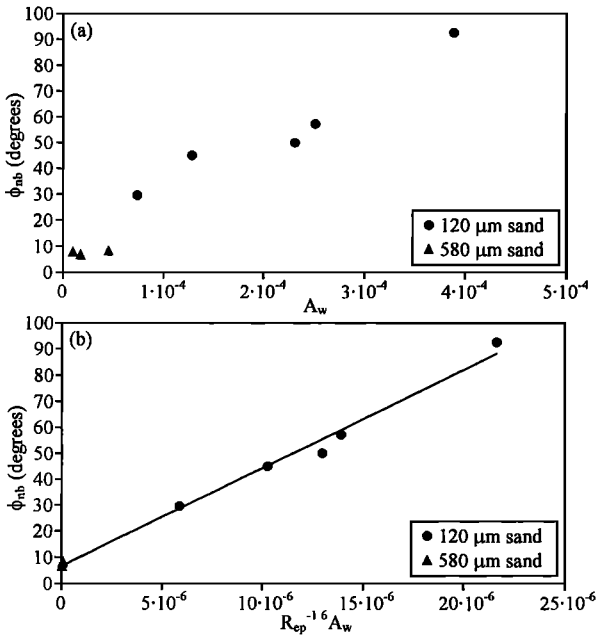


Figure 9. Phase lag of near-bed concentration as a function of (a)  $A_w$  and (b)  $R_{ep}^{-1.6} A_w$ .

the pulse, the 120  $\mu\text{m}$  sand is immersed within the sublayer throughout the pulse. If the sand is immersed within the viscous sublayer, it can still be entrained. However, the larger the ratio of the sand diameter to the viscous sublayer thickness is, the more easily the sand is entrained.

A bed composed of 120  $\mu\text{m}$  sand is not as rough as one composed of 580  $\mu\text{m}$  sand, and turbulent fluctuations produced by the bed may be lower. Reduction in bed roughness is also likely to delay the onset of turbulence. The shear stress pulse used to develop Figure 10b is also used to compare the roughness parameters ( $k_s^+$ ) for each of the sediment sizes. The 120  $\mu\text{m}$  and 580  $\mu\text{m}$  sand beds subjected to the pulse have the roughness parameter time series shown in Figure 10c. The roughness parameters  $k_s^+ = 5$  and  $k_s^+ = 70$  indicate the boundaries between the smooth, transitionally rough, and rough regimes and are also shown in Figure 10c. While the 120  $\mu\text{m}$  sand bed can be considered smooth for the entire test, the 580  $\mu\text{m}$  sand bed is transitionally rough for most of the test. The two influences of sand grain diameter demonstrated in Figure 10 both produce a larger phase lag for smaller particles.

Flow conditions also affect phase lag. The phase lag is greater for the 120  $\mu\text{m}$  tests, but the shear stresses and flow velocities are also lower. Since the flow does not have as much energy for the 120  $\mu\text{m}$  sand tests, the turbulence will be

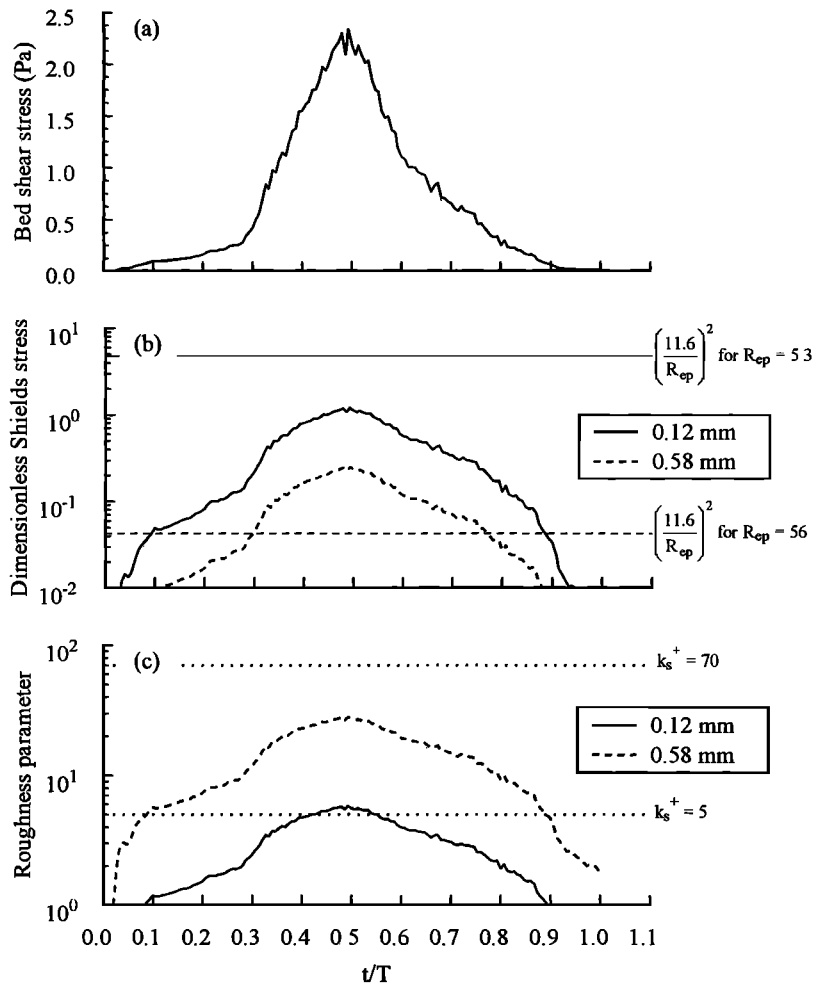
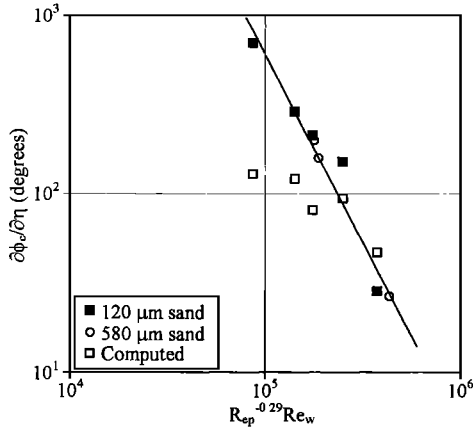
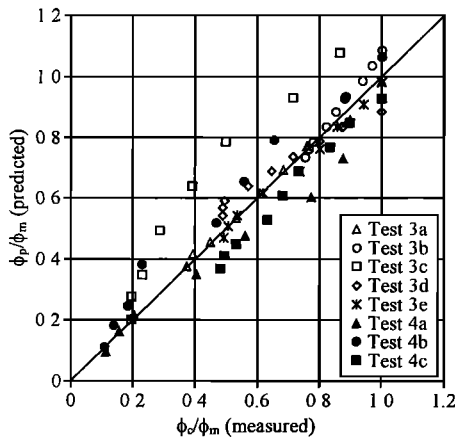


Figure 10. (a) Shear stress time series imposed on sand bed, (b) corresponding Shields stress time series, and (c) roughness parameter time series for 120  $\mu\text{m}$  and 580  $\mu\text{m}$  sand beds.



**Figure 11.** Slope of the phase lag profiles shown in Figure 8 given as a function of wave Reynolds number and particle Reynolds number.

weaker. This will increase the time lag since turbulence is what carries the sand from the bed to the height at which entrainment rate is measured. *Ramaprian and Tu* [1982] have investigated the propagation time of turbulence for periodic flow in a smooth pipe. They found that the propagation time is inversely related to the magnitude of the average shear velocity. For the 120 μm sand tests the shear velocity is significantly less than for the 580 μm sand tests, resulting in a longer propagation time. Assuming that the experimental results of *Ramaprian and Tu* are also valid for duct flows, a rough estimate of the time required for turbulence to propagate from the bed to the near-bed reference level can be calculated. This turbulence propagation time, denoted  $\Delta t_p$ , is given for each of the unsteady flow tests in Table 2. For comparison, time lags of the near-bed concentration ( $\Delta t_c$ ) have also been given in Table 2. Though the values of  $\Delta t_p$  given are only approximate, they reveal how turbulence propagation time can influence the time lag of near-bed concentration and entrainment rate. Turbulence propagation times are greater for the 120 μm sand tests than for the 580 μm sand tests, providing a possible explanation for the longer time lags observed for the 120 μm sand. Note that entrainment is caused primarily by large scales of turbulence, and  $\Delta t_p$  is calculated from all of the turbulence



**Figure 12.** Comparison of measured and predicted phase lags of peak concentration.

scales. Thus, even if  $\Delta t_p$  can be accurately determined, it does not give the exact propagation time of the entrained sediment.

Prediction of the phase lags given in Figure 9a can be improved if  $A_w$  is modified using the particle Reynolds number. In Figure 9b the phase lag of near-bed concentration was plotted as a function of  $R_{ep}^m A_w$ , where the optimal value of  $m$  was found to be  $-1.6$ . A curve fit of the data is also shown in Figure 9b and is given by

$$\phi_{nb} = 3.8 \times 10^6 (R_{ep}^{-1.6} A_w) + 6.6. \quad (25)$$

Gradients of the phase lag curves shown in Figure 8 also vary between tests. The amount of time that it takes for suspended sediment to be carried from near the bed to a point farther from the bed depends on the level of turbulence. Consequently, the wave Reynolds number might be a good indicator of the propagation time of the suspended sediment. Figure 11 gives the gradient of the phase lag of peak concentration with respect to elevation as a function of  $R_{ep}^n Re_w$ . If the effect of  $R_{ep}$  is ignored, the 120 μm sand data and the 580 μm sand data fall on two separate curves that have the same slope. Setting  $n$  equal to  $-0.29$  collapses the curves. A curve fit to the measured data is

$$\frac{\partial \phi_c}{\partial \eta} = 1.92 \times 10^6 (R_{ep}^{-0.29} Re_w)^{-2.1}, \quad (26)$$

where  $\partial \phi_c / \partial \eta$  is given in degrees per unit elevation. Sand diameter continues to play an important role once the sediment is suspended. For similar Reynolds numbers,  $\partial \phi_c / \partial \eta$  is much larger for the 580 μm sand than for the 120 μm sand. Thus, for similar flow conditions the 120 μm sand is more rapidly transported from the location of entrainment to the outer flow. Figure 11 also shows the values of  $\partial \phi_c / \partial \eta$  computed by numerically solving the advection-diffusion equation (8) for the 120 μm sand tests. These computations are discussed more in section 7.3.

In Figure 12, measured phase lags of peak concentration are compared with phase lags predicted using the results shown in Figures 9b and 11. The predicted ( $\phi_p$ ) and measured ( $\phi_c$ ) phase lags for each test are divided by the phase lag measured at  $\eta = 0.42$  ( $\phi_m$ ). This method is adopted so that results from all of the tests can be compared on one graph.

### 7.2. Phase Lags of Peak Entrainment Measurements

Figure 13 shows the phase lag of the peak entrainment ( $\phi_E$ ) as a function of  $A_w$  and  $R_{ep}$ . Phase lags of the peak near-bed

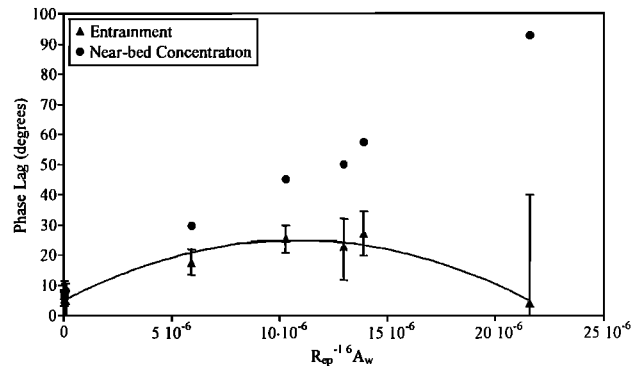


**Figure 13.** Phase lag of entrainment and near-bed concentration as a function of  $R_{ep}^{-1.6} A_w$ .

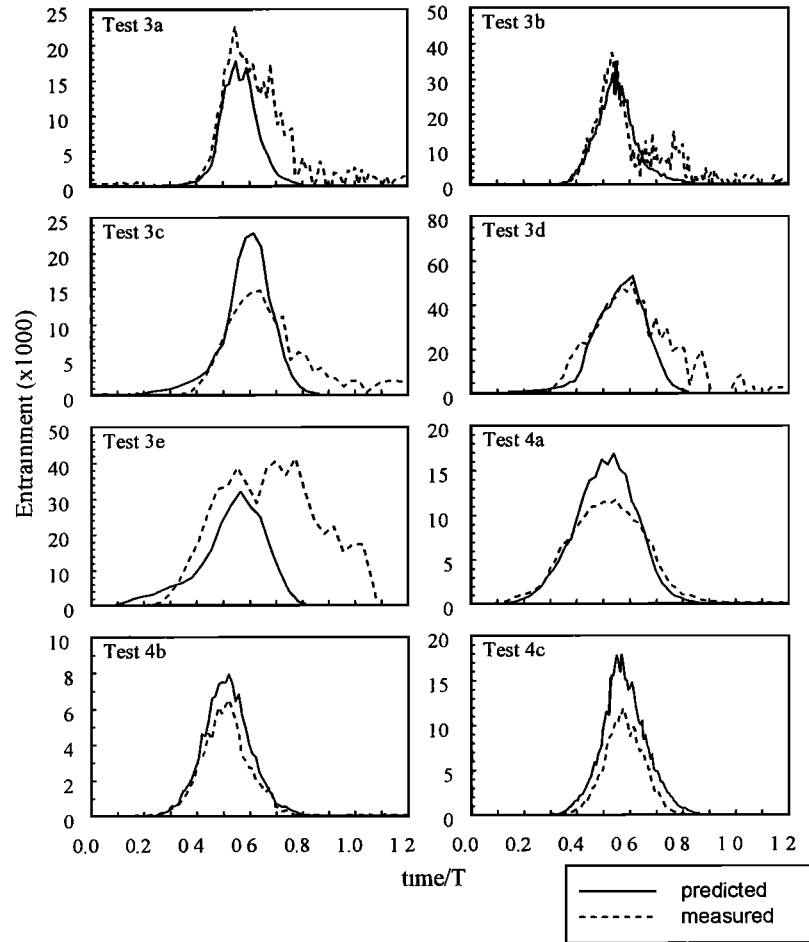


**Figure 14.** Comparison of predicted and measured entrainment time series for unsteady pulse tests. Phase lags have been used to correct the timing of predictions.

concentration are shown in the same diagram for comparison. Figure 13 indicates that at low accelerations the phase lag of the entrainment rate is similar to the phase lag of the near-bed concentration. This is expected since entrainment rate and near-bed concentration are the same for quasi-steady flows. As acceleration increases, however, the upward flux of sediment is no longer balanced by sediment deposition, and the phase lag of the entrainment rate becomes less dependent on the phase lag of the near-bed concentration. For very high accelerations the amount of sediment within the control volume may be changing rapidly even if the near-bed concentration remains small. The time at which the peak entrainment rate occurs in each of the tests is not precise (peak concentrations, however, are well defined), and estimates of the uncertainty associated with each peak entrainment phase lag measurement are shown in Figure 13. In general, phase lag uncertainty estimates increase with acceleration. Some of the entrainment time series were asymmetric, and the measured phase lag of the peak entrainment does not necessarily lie at the center of the range of uncertainty.

Here  $\tau_E$  is the time lag of entrainment rate after bed shear stress and is given as

$$\tau_E = \frac{\phi_E}{360} T. \quad (27)$$

In order to compute the entrainment rate at the time  $t$ , the value of  $u_*$  measured at the time  $t - \tau_E$  is introduced into (4) and (5). Introducing a time lag does not change the shape of the entrainment rate pulse; it only changes the time at which the pulse occurs.

A quadratic was fit to the phase lag measurements so that comparisons between predicted and measured entrainment rates could be made. The curve fit is

$$\phi_E = -2 \times 10^{11} (R_{ep}^{-1.6} Re_w)^2 + 4 \times 10^6 (R_{ep}^{-1.6} Re_w) + 5.0. \quad (28)$$

Considering the accuracy of the data in Figure 13, (28) is not a definitive relation between the phase lag of entrainment, shear stress acceleration, and particle Reynolds number, but it can be used to predict the entrainment rate phase lags of each of the tests given in Table 2. Figure 14 shows the predicted and measured entrainment rate time series of each of the pulse tests with the phase lag of entrainment taken into account. Comparison of Figures 7 and 14 demonstrates that phase lag corrections improve entrainment rate predictions considerably.

### 7.3. Sediment Load Calculations

It is useful to explore how the choice of boundary conditions affects suspended sediment load calculations. In this way the

importance of time lags can be assessed. The total suspended sediment load per unit width of duct ( $Q_s$ ) is

$$Q_s = \int_{t_s}^{t_e} \int_{b_0}^{b_1} \rho_s \bar{c} \bar{u} \, dz \, dt, \quad (29)$$

where  $\rho_s$  is the density of the sediment and  $t_s$  and  $t_e$  indicate the start and end of the test, respectively. In order to solve (29), the time variation of vertical velocity and concentration profiles must be known. Equation (8) is used to obtain concentration profiles. The flow is uniform and two-dimensional, and ensemble-averaged vertical velocities are small, so (8) becomes

$$\frac{\partial \bar{c}}{\partial t} + \frac{\partial}{\partial z} (\langle u'_3 c' \rangle - v_s \bar{c}) = 0. \quad (30)$$

The ensemble-averaged Reynolds concentration flux is modeled as

$$\langle u'_3 c' \rangle = -\varepsilon_s \frac{\partial \bar{c}}{\partial z}, \quad (31)$$

where  $\varepsilon_s$  is the eddy diffusivity of the sediment.

In the steady flow tests, vertical concentration profiles of the 120  $\mu\text{m}$  sand were successfully predicted by assuming that eddy diffusivity and turbulent eddy viscosity are equal [see *Admiraal*, 1999]. Assuming this is also true of unsteady flows, the final form of (30) is

$$\frac{\partial \bar{c}}{\partial t} = \frac{\partial}{\partial z} \nu_t \frac{\partial \bar{c}}{\partial z} + v_s \frac{\partial \bar{c}}{\partial z}, \quad (32)$$

where  $\nu_t$  is the turbulent eddy viscosity. A finite difference method was applied to (32), and vertical profiles of sediment concentration were computed as a function of time for tests 3a through 3e. Instantaneous turbulent eddy viscosity distributions were assumed to be the same as those in an equivalent two-dimensional, steady duct flow. Three different boundary conditions for sediment concentration were attempted, resulting in three solutions for each test. The first boundary condition investigated was the near-bed concentration. In this case, (13) was assumed to be valid and the García-Parker relation was used to calculate near-bed concentration. For the second boundary condition the entrainment rate was specified. The García-Parker relation was again used to determine the entrainment rate. The third boundary condition was the time-delayed entrainment rate. Time lags measured for each test were applied to the entrainment rate to get the time-delayed entrainment rate. Since entrainment is caused by turbulence, time delays applied to the entrainment rate were also applied to the eddy viscosity distribution. All three boundary conditions were calculated from shear stress distributions measured during the tests.

The vertical velocity profile was assumed to be uniform and was set equal to the measured centerline velocity (the log law is not necessarily valid in the present set of unsteady flows). In Table 3, estimates of  $Q_s$  are given for tests 3a through 3e and the three boundary conditions. For the test conditions investigated, using an entrainment rate boundary condition instead of time-delayed entrainment rate can increase suspended load estimates by more than 15%. Using near-bed concentration instead of time-delayed entrainment rate can double suspended load estimates. When the near-bed concentration boundary condition is used, suspended load is always overpre-

dicted, first, because the peak concentration predicted near the bed is greater than the actual concentration, and second, because the peak concentration near the bed is forced to occur at nearly the same time as peak velocity. Measurements indicate that peak concentrations occur well after the peak velocity, reducing the overall sediment load. The entrainment rate boundary condition (without the time delay) also predicts the arrival of the peak near-bed concentration prematurely. However, the entrainment rate boundary condition still works significantly better than the near-bed concentration boundary condition.

Sediment loads calculated from concentration and velocity measurements are also given in Table 3. Differences between measured and computed loads result not only from the choice of boundary conditions but also from measurement error and inaccuracy of the García-Parker relation. Thus the measurements do not always indicate which boundary condition is best. However, in cases where measured and predicted entrainment rates agree, the time-delayed entrainment rate boundary condition performs best. For instance, in test 3d the measured and predicted entrainment rates are similar, and the time-delayed entrainment boundary condition provides the best estimate of the total suspended load.

Although results given in Table 3 show the importance of choosing the appropriate near-bed boundary condition, it should be noted that the actual distribution of turbulent eddy viscosity is unknown and that delays in turbulence propagation can further reduce sediment loads. Furthermore, the assumption that eddy diffusivity and eddy viscosity are the same does not work well for predicting vertical concentration profiles of the 580  $\mu\text{m}$  sand, even in steady flows [*Admiraal*, 1999]. Consequently, suspended load was not calculated for the 580  $\mu\text{m}$  sand tests.

Advection and diffusion of the sediment takes time, resulting in delays between the peak near-bed concentration and peak concentrations higher above the bed. Phase lags of peak concentration calculated using (32) were used to determine  $\partial \phi_c / \partial \eta$  for tests 3a through 3e. The computed gradients were plotted with the measured gradients in Figure 11. The results shown in Figure 11 indicate that at high wave Reynolds numbers (low acceleration and high peak velocity), a quasi-steady turbulence model adequately predicts advection and diffusion times of the sediment. However, for low wave Reynolds numbers the quasi-steady model largely underpredicts the propagation time of the sediment. At low wave Reynolds numbers the eddy viscosity distribution may be significantly different than modeled.

## 8. Conclusions

This paper explores the effects of flow unsteadiness on the process of suspended sediment entrainment and transport. A variety of experiments are reported, including both steady and unsteady flow tests above mobile beds composed of either 120  $\mu\text{m}$  or 580  $\mu\text{m}$  diameter sand. Results of steady flow tests are shown in Figure 4 and indicate that the García-Parker relation can adequately predict entrainment rates for Reynolds numbers (based on duct height and centerline velocity) as high as  $1.6 \times 10^5$ .

When sediment is suspended by unsteady flow pulses, peak concentrations of suspended sediment lag behind the peak shear stress. The time lag of the peak concentration increases with distance from the bed. Phase lag of the near-bed concen-

tration is dependent on both sediment size and flow acceleration, and a relation based on the particle Reynolds number and the shear velocity acceleration is given for predicting near-bed concentration (equation (25)) in unsteady pulse flows. The transport of sediment from near the bed to farther from the bed is dependent on turbulence levels, and a relation based on the particle and wave Reynolds numbers (equation (26)) is given for predicting the phase lags of peak concentrations farther from the bed. The second relation should be treated cautiously since the wave Reynolds number (unlike the flow Reynolds number) does not take boundary layer thickness into account, and turbulence levels depend on boundary layer thickness.

Experiments show that the García-Parker relation works for unsteady flows with dimensionless shear velocity accelerations (see (18)) as high as  $4 \times 10^{-4}$  and wave Reynolds numbers (see (17)) as high as  $1.4 \times 10^6$ . However, a time delay must be applied to the predicted entrainment rate since there is a time lag between bed shear stress and entrainment. The time lag is attributable to a time lag between flow velocity and the production and propagation of turbulence. Like the phase lag of near-bed concentration, the phase lag of the entrainment rate depends on the particle Reynolds number and the dimensionless acceleration of shear velocity. Figures 7 and 14 demonstrate how implementing the phase lag of entrainment can improve entrainment rate predictions.

Predictions and measurements of the total amount of entrained sediment are also compared. The García-Parker relation adequately predicts the magnitude of entrainment rate, even for the flows with the highest accelerations. Predicted and measured entrainment rates are not entirely in agreement during flow deceleration, especially for fine sediment. Residual turbulence may reduce fall velocity, increase entrainment rates, or both. The resulting disparity between predicted and measured entrainment rates increases with increasing flow deceleration since the decay of the turbulence appears to be independent of the flow deceleration rate. Attempts to correct the entrainment relation using turbulence variables are not made since measurements of near-bed turbulence are not possible with the present instrumentation.

Numerical solutions of the advection-diffusion equation (8) for five of the unsteady flow tests demonstrate the importance of choosing an appropriate near-bed boundary condition. There are significant differences between total suspended loads computed using near-bed concentration, entrainment rate, and time-delayed entrainment rate boundary conditions. For unsteady flows the entrainment rate is a more appropriate boundary condition than the near-bed concentration, but if phase differences between flow velocity and sediment entrainment are ignored, total suspended load can still be over-predicted or under-predicted. Results of the numerical model also show that the advection-diffusion equation can adequately predict the propagation time of the sediment for high wave Reynolds numbers. However, proper solution of (8) requires knowledge of the turbulence distribution in the flow; this distribution is not easily ascertained.

The unsteady flow experiments presented in this paper begin with the flow at rest. Often, the flow is moving or turbulent prior to the arrival of an unsteady flow pulse. If this is the case, the relative importance of the background flow must be evaluated. A small increase in shear velocity significantly increases the entrainment rate (see Figure 4); therefore, when the peak unsteady flow is substantially larger than the background flow,

the background flow has little effect on the entrainment process. Phase lags observed between bed shear stress and peak near-bed concentration are similar to those observed in comparable periodic flows, and it is expected that delays in turbulence production and propagation are also similar. Thus it is likely that unsteady periodic and nonperiodic flows will exhibit similar entrainment behavior.

**Acknowledgments.** The support of the U.S. Army Corps of Engineers, Waterways Experiment Station (grant DACW39-95-K-0101) and the U.S. Army Research Office (grant DAAH04-96-1-0132) is gratefully acknowledged. The authors are especially thankful for the generosity and helpfulness of Alex Hay. Finally, the authors appreciate the constructive remarks of Mark Schmeckle and two anonymous reviewers.

## References

- Admiraal, D., Hot film shear stress measurements in laminar and turbulent flows, in *Proceedings of the John F. Kennedy Student Paper Competition and Specialty Seminar Summaries*, pp. 61–66, Am. Soc. of Civ. Eng., Reston, Va., 1997.
- Admiraal, D., Entrainment of sediment by unsteady turbulent flows, Ph.D. dissertation, Dep. of Civ. and Environ. Eng., Univ. of Ill. at Urbana-Champaign, 1999.
- Admiraal, D., and M. García, Laboratory measurement of suspended sediment concentration using an acoustic concentration profiler (ACP), *Exp. Fluids*, in press, 1999.
- Akiyama, J., and Y. Fukushima, Entrainment of noncohesive sediment into suspension, in *3rd International Symposium on River Sedimentation*, edited by S. Y. Wang, H. W. Shen, and L. Z. Ding, pp. 804–813, Univ. of Miss., University, 1986.
- Boillat, J.-L., and W. H. Graf, Settling velocities of spherical particles in turbulent media, *J. Hydraul. Res.*, 20(5), 395–413, 1982.
- Celik, I., and W. Rodi, A deposition-entrainment model for suspended sediment transport, *Rep. SFB 210/T/6*, Univ. Karlsruhe, Karlsruhe, Germany, 1984.
- Davies, A. G., Effects of unsteadiness on the suspended sediment flux in co-linear wave-current flow, *Cont. Shelf Res.*, 15(8), 949–979, 1995.
- Einstein, H. A., The bed load function for sediment transportation in open channels, *Tech. Bull. 1026*, Soil Conserv. Serv., U.S. Dep. of Agric., Washington, D. C., 1950.
- Engelund, F., and J. Fredsøe, A sediment transport model for straight alluvial channels, *Nord. Hydrol.*, 7(5), 293–306, 1976.
- Engelund, F., and J. Fredsøe, Hydraulic theory of alluvial rivers, *Adv. Hydrosci.*, 13, 187–215, 1982.
- Fredsøe, J., and R. Deigaard, *Mechanics of Coastal Sediment Transport*, World Sci., River Edge, N. J., 1992.
- García, M. H., and G. Parker, Entrainment of bed sediment into suspension, *J. Hydraul. Eng.*, 117(4), 414–435, 1991.
- García, M., F. López, and Y. Niño, Characterization of near-bed coherent structures in turbulent open channel flow using synchronized high-speed video and hot-film measurements, *Exp. Fluids*, 19, 16–28, 1995.
- Hay, A. E., Sound scattering from a particle-laden turbulent jet, *J. Acoust. Soc. Am.*, 90(4), 2055–2074, 1991.
- Horikawa, K. A., A. Watanabe, and S. Katori, Sediment transport under sheet flow condition, in *Proceedings of the Eighteenth International Coastal Engineering Conference*, 1335–1352, Am. Soc. of Civ. Eng., Reston, Va., 1982.
- Inman, D. L., and A. J. Bowen, Flume experiments on sand transport by waves and currents, in *Proceedings of the Eighth Conference on Coastal Engineering*, pp. 137–150, Am. Soc. of Civ. Eng., Reston, Va., 1962.
- Itakura, T., and T. Kishi, Open channel flow with suspended sediments, *J. Hydraul. Div., Am. Soc. Civ. Eng.*, 106(8), 1325–1343, 1980.
- Lapointe, M., Burst-like sediment suspension events in a sand bed river, *Earth Surf. Processes Landforms*, 17, 253–270, 1992.
- Ludwick, J. C., and G. W. Domurat, A deterministic model of the vertical component of sediment motion in a turbulent fluid, *Mar. Geol.*, 45, 1–15, 1982.
- Menendez, A. N., and B. R. Ramaprian, The use of flush-mounted

- hot-film gauges to measure skin friction in unsteady boundary layers, *J. Fluid Mech.*, 161, 139–159, 1985.
- Mizushima, T., T. Maruyama, and H. Hirasawa, Structure of the turbulence in pulsating pipe flows, *J. Chem. Eng. Jpn.*, 8(3), 210–216, 1975.
- Murray, S. P., Settling velocities and vertical diffusion of particles in turbulent water, *J. Geophys. Res.*, 75(9), 1647–1654, 1970.
- Nezu, I., and H. Nakagawa, *Turbulence in Open-Channel Flows*, A. A. Balkema, Broomfield, Vt., 1993.
- Nielsen, P., Three simple models of wave sediment transport, *Coastal Eng.*, 12, 43–62, 1988.
- Nielsen, P., *Coastal Bottom Boundary Layers and Sediment Transport*, World Sci., River Edge, N. J., 1992.
- Niño, Y., and M. H. García, Experiments on particle-turbulence interactions in the near-wall region of an open channel flow: Implications for sediment transport, *J. Fluid Mech.*, 326, 285–319, 1996.
- Parker, G., Self-formed straight rivers with equilibrium banks and mobile bed, 1, The sand-silt river, *J. Fluid Mech.*, 89, 109–125, 1978.
- Ramaprian, B. R., and S. W. Tu, Study of periodic turbulent pipe flow, *Rep. 238*, Iowa Inst. of Hydraul. Res., Iowa City, 1982.
- Rodríguez, J., Wall shear stress measurements in unsteady turbulent flow, in *Proceedings of the John F. Kennedy Student Paper Competition and Specialty Seminar Series*, pp. 67–72, Am. Soc. of Civ. Eng., Reston, Va., 1997.
- Rouse, H., Experiments on the mechanics of sediment suspension, in *Proceedings Fifth International Congress of Applied Mechanics*, pp. 550–554, John Wiley, New York, 1939.
- Rouse, H., *Fluid Mechanics for Hydraulic Engineers*, Dover, Mineola, N. Y., 1961.
- Schlichting, H., Experimentelle untersuchungen zum rauhgkeitsproblem, *Ing-Arch.*, 7, 1–34, 1936.
- Smith, J. D., and S. R. McLean, Spatially averaged flow over a wavy surface, *J. Geophys. Res.*, 82(12), 1735–1746, 1977.
- Soulsby, R. L., R. Atkins, and A. P. Salkield, Observations of the turbulent structure of a suspension of sand in a tidal current, paper presented at Euromech 215, Mechanics of Sediment Transport in Fluvial and Marine Environments, Eur. Mech. Soc., Genoa, Italy, Sept. 15–19, 1987.
- Sutherland, A. J., Proposed mechanism for sediment entrainment by turbulent flows, *J. Geophys. Res.*, 72(24), 6183–6194, 1967.
- van Rijn, L. C., Sediment transport, 2, Suspended load transport, *J. Hydraul. Eng.*, 110(11), 1613–1641, 1984.
- Wang, L. P., and M. R. Maxey, Settling velocity and concentration distribution of heavy particles in homogeneous, isotropic turbulence, *J. Fluid Mech.*, 256, 27–68, 1993.
- Zyserman, J. A., and J. Fredsøe, Data analysis of bed concentration of suspended sediment, *J. Hydraul. Eng.*, 120(9), 1021–1042, 1994.

---

D. M. Admiraal, Department of Civil Engineering, University of Nebraska at Lincoln, W338 Nebraska Hall, Lincoln, NE 68588-0531. (dadmiraa@unlnotes.unl.edu)

M. H. García and J. F. Rodríguez, Hydrosystems Laboratory, Department of Civil and Environmental Engineering, University of Illinois at Urbana-Champaign, 205 N. Matthews Avenue, Urbana, IL 61801. (mhgarcia@uiuc.edu; jfrodrig@uiuc.edu)

(Received February 1, 1999; revised July 23, 1999; accepted July 23, 1999.)